An adaptive noise-blind-separation algorithm for ptychography

Li Liu [a], Wenjie Li [a], Lei Zhong [a], Honggang Gu [a,b,c,*], Shiyuan Liu [a,b,*]

[a] *State Key Laboratory of Intelligent Manufacturing Equipment and Technology, Huazhong University of Science & Technology, Wuhan 430074, China*
[b] *Optics Valley Laboratory, Wuhan 430074, China*
[c] *Guangdong HUST Industrial Technology Research Institute, Guangdong Provincial Key Laboratory of Manufacturing Equipment Digitization, Dongguan, Guangdong 523003, China*

ARTICLE INFO

ABSTRACT

Noise, one of the severe challenges in phase retrieval, may bring the algorithms to fall into local minima or even disrupt the convergence, thereby adversely affecting the imaging quality and convergence efficiency in the ptychography. Here, we propose an adaptive noise-blind-separation (aNBS) algorithm to deal with mixed noises of different types without sensitivity discrepancy in ptychography. In the aNBS algorithm, apart from the coherent probe of the illumination wavelength, virtual probes of different wavelengths are introduced to capture the noise energies, and the coupling mixed noises are adaptively blind-separated into the virtual noise probes in ptychography. The proposed algorithm can blindly separate coherent diffraction signals and noises without requiring additional regularization constraints, noise prior assumptions or dynamic iteration parameters. Simulations and experiments are comparatively conducted with the momentum-accelerated ptychographical iterative engine algorithm without dealing with noises and the least-square maximum-likelihood ptychographical iterative engine algorithm using a mixed Poisson-Gaussian likelihood model. Results indicate that the aNBS-based ptychography significantly enhances the convergence robustness when the noise intensity increases by more than two orders of magnitude. Compared with existing methods, the proposed aNBS algorithm demonstrates superior robustness and generality for the phase retrieval in coherent diffraction imaging and can be widely applied to various fields, such as ptychography, holography, and tomography.

1. Introduction

Due to the inherent constraints of fabricating optical lenses with superior imaging qualities and larger numerical apertures, conventional optical microscopes have encountered difficulties in meeting the imaging demands of emerging fields, such as cell biology [1], condensed matter physics [2], and emerging materials science [3]. Ptychography, a lensless imaging technique, inherently falls into the category of phase retrieval. Rodenburg et al. proposed the ptychographical iteration engine (PIE [4]) for the first time to retrieve phase through alternating projections in ptychography. Subsequently, they extended the algorithm to address blind problems without the prior probe (i.e., the extended PIE, ePIE [5]) and enhanced both the convergence robustness (i.e., the regularized PIE, rPIE [6]) and the convergence speed (i.e., the momentum-accelerated PIE, mPIE [6]). Simultaneously, alternative phase retrieval algorithms, such as the difference map [7], the relaxed averaged alternating reflections [8] and others [9,10], based on the projection and reflection principle, have also been proposed, and these

approaches have further refined the results in blind ptychography, exhibiting increased convergence speeds and stronger abilities to escape the local minima compared with PIE-kernel ptychography.

Besides the iterative projection algorithms [4–11], several innovative proximal algorithms also have also been introduced in the field of ptychography, such as proximal gradient methods [12–14] and alternating direction methods of multipliers (ADMM) [15–17]. All these algorithms, including projection algorithms and proximal algorithms, are also referred to as "class 1 algorithms" [18]. Recently, more and more researchers have focused on the noise in "class 2 algorithms [19–24]", which constitutes the most fundamental relaxation of the "class 1 algorithms", and reconstruction algorithms for ptychographic noises have been developed with an emphasis on enhanced robustness and generality. For instance, by establishing statistical noise models, the available results were effectively extracted by Thibault et al. [25] and Odstrčil et al. [26] from the raw ptychography data based on maximum-likelihood estimation, which minimized the negative logarithm of the likelihood function to maximize the likelihood of measured

---

intensity or amplitude for the noise distribution functions essentially. However, these maximum-likelihood algorithms often require prior assumptions [27,28] or appropriate regularization requirement [29] to ensure the iterative convergence. Zhang et al. [30] removed the regularization demand by combining generalized Anscombe transform approximation of mixed Poisson-Gaussian models with maximum-likelihood principle, but the algorithm still needed prior assumptions model to approximate noises. By further combining variance-stabilizing transforms with maximum-likelihood estimation method, Konijnenberg et al. [31] improved the cost function of ptychography using the adaptive intensity constraint, which made the algorithm more general by removing the constraint of noise prior assumptions. Due to the presence of noise, the ptychography has been actually transformed into a more complicated non-convex optimization problem, and Zuo et al. [32] and Wu et al. [33] applied an adaptive step size method to suppress the decline of convergent accuracies. Those noise-optimization algorithms that minimize the ptychographic cost function can only reduce the impact of noises on the reconstruction accuracy but cannot completely separate the noises from the convergent images.

Recently, noise-separation algorithms have attracted great interest from researchers in the field of ptychography. As presented by Wang et al. [34], the mixed noises, approximated as the background noise, were directly removed from the measurement signals by using the minimization method, threshold method, and localized erasing method, while these methods may directly cause the loss of high spatial frequencies in diffraction signals. By combining guided filtering with the ePIE algorithm, an adaptive guided filtering method to inhibit the background noise was proposed by Qiao et al. [35], but their method still needed to adjust the constraint factor in the iteration process yet. A more advanced algorithm to optimize and remove mixed noise in ptychography was also presented by Chang et al. [36] based on the forward physical model of background noise and the shift-Poisson method with the maximum a posteriori estimation.

In this paper, an innovative adaptive noise-blind-separation (aNBS) algorithm is presented to effectively deal with mixed noises in ptychographic reconstructions while maintaining consistent sensitivity to different noise types. By constructing scalar diffraction propagation of the virtual probes and the illumination probe based on the "Fractional" Fourier transform [37], the coupled mixed noises in the diffraction signals could be adaptively separated into the noise probes in the ptychographic iterative process. Unlike existing algorithms [6,26], the proposed aNBS algorithm does not need additional regularization nor noise prior assumptions. Furthermore, the algorithm does not need to adjust the iteration parameters [35] in the convergence process and can blindly separate different mixed noises without any sensitivity discrepancy as the noise intensity increases by several orders of magnitude. These advantages make the proposed aNBS algorithm more robust and general than state-of-the-art algorithms, enabling its application in various fields of coherent diffraction imaging including the ptychography, holography, and tomography.

2. Theory and algorithm

As a fundamental optical propagation model, the scalar diffraction propagation based on the discrete Fourier transform has been widely applied in holography [37,38], ptychography [18,39,40], ankylography [41,42] and tomography [24]. Limited by the scale constraints of the sampling interval and optical field size between the source plane and the observation plane [43], the angular spectrum propagation and the Fresnel integral model only adapt to the near-field optical diffraction. However, in the far-field optical diffraction, the Fraunhofer integral, which maintains the constant factor (λz) of a scale constraint between the source plane and the observation plane, encounters difficulties in upholding the alignment of the sampling interval and optical field size during multi-wavelength propagation.

2.1. The variable scale Fresnel convolution integral

The Fresnel convolution integral, based on the "Fractional" Fourier transform [37], breaks the sampling interval and optical field size constraints imposed by the Fresnel and Fraunhofer diffraction integrals, and thus provides an impeccable solution for the free-space propagation of diffraction fields over multiple wavelengths. The conventional Fresnel diffraction integral can be expressed by

$$u_2(x_2, y_2) = \frac{\exp(ikz)}{i\lambda z} \int \int u_1(x_1, y_1)\exp\left\{\frac{ik}{2z}\left[(x_2 - x_1)^2 + (y_2 - y_1)^2\right]\right\}dx_1 dy_1, \tag{1}$$

where, k is the wave number, λ is the optical vacuum wavelength, z is the propagation distance between the source plane and the observation plane, and x_1, y_1 and x_2, y_2 are the coordinate variables of the source plane and the observation plane respectively, $u_1(x_1, y_1)$ and $u_2(x_2, y_2)$ are the optical distributions of the source plane and the observation plane respectively.

By introducing the scaling factors m and n, which are not limited to the λz scale constraint in the Fraunhofer diffraction integral, the Fresnel integral on Eq. (1) can be rewritten as

$$u_2(x_2, y_2) = \frac{\exp(ikz)}{i\lambda z} \int \int u_1(x_1, y_1)\exp\left\{\frac{ik}{2z}\left[\left(m\left(\frac{x_2}{m} - x_1\right)^2 + \left(1 - \frac{1}{m}\right)x_2^2 + \right.\right.\right.$$
$$\left.\left.(1 - m)x_1^2 + \left(n\left(\frac{y_2}{n} - y_1\right)^2 + \left(1 - \frac{1}{n}\right)y_2^2 + (1 - n)y_1^2\right)\right]\right\}dx_1 dy_1$$
$$= \frac{\exp(ikz)}{i\lambda z}\exp\left\{\frac{ik}{\lambda z}\left[\left(1 - \frac{1}{m}\right)x_2^2 + \left(1 - \frac{1}{n}\right)y_2^2\right]\right\} \int \int u_1(x_1, y_1)\times$$
$$\exp\left\{\frac{ik}{2z}\left[(1 - m)x_1^2 + (1 - n)y_1^2\right]\right\}\exp\left[\frac{ikm}{2z}\left(\frac{x_2}{m} - x_1\right)^2 + \frac{ikn}{2z}\left(\frac{y_2}{n} - y_1\right)^2\right]dx_1 dy_1, \tag{2}$$

assuming that the intermediate variable $u(x_1, y_1)$ related to the source plane optical field distribution can be expressed as

$$u(x_1, y_1) = u_1(x_1, y_1)\exp\left\{\frac{ik}{2z}\left[(1 - m)x_1^2 + (1 - n)y_1^2\right]\right\}, \tag{3}$$

the variable scale Fresnel convolution integral $u_2(x_2', y_2')$ can be obtained as

$$u_2(x_2', y_2') = \frac{\exp(ikz)}{i\lambda z}\exp\left[\frac{ik}{2z}\left((m^2 - m)x_2'^2 + (n^2 - n)y_2'^2\right)\right]\times$$
$$\int \int u(x_1, y_1) \times h(x_2' - x_1, y_2' - y_1)dx_1 dy_1, \tag{4}$$

where, the scaled sampling interval x_2' and y_2' of the observation plane and the convolution function $h(x_2'$-x_1, y_2'-$y_1)$ can be calculated according to Eq. (2) as respectively

$$x_2' = \frac{x_2}{m}, \quad y_2' = \frac{y_2}{n}, \tag{5}$$

$$h(x_2' - x_1, y_2' - y_1) = \exp\left[\frac{ikm}{2z}(x_2' - x_1)^2 + \frac{ikn}{2z}(y_2' - y_1)^2\right] \tag{6}$$

By carefully selecting appropriate scale factors (m and n) on the source plane to account for varying wavelengths, the optical field distribution at the observation plane can be calculated using the "Fractional" Fourier transform in conjunction with the Fresnel convolution integral. Compared with conventional Fresnel and Fraunhofer diffraction integrals, the computational complexity of the variable scale Fresnel convolution integral is maintained at a comparable level. Therefore, the method provides a fast and effective solution for tackling the complexities of diffraction propagation involving multi-wavelength optical fields.

2.2. The aNBS algorithm for mixed noises

The experimental setup and iterative algorithms of ptychography have been described in previous literature [18,39], and will not be discussed in detail here. Diffraction signals are collected at different offsets between the probe and the specimen in finite offsets S, and the jth diffraction signal I_{q_j} is recorded according to Eq. (7)

$$I_{q_j} = \left| F\left[P_r \times O_{r+r_j} \right] \right|^2, \quad \forall r_j \in S, \tag{7}$$

where, q and r are reciprocal-space and real-space coordinate variables, P_r is the complex function of the illumination beam called the "probe" and O_{r+r_j} is the complex refractive function of the specimen called the "object". r_j is the jth object relative offset (x_j, y_j) in the set S, and F is the two-dimensional scalar diffraction model. According to the real-space overlap constraints and the reciprocal-space modulus constraints, the ptychographic phase retrieval minimizes the Euclidean norm ε as

$$\varepsilon = \arg \min_{P_r, O_{r+r_j}} \sum_j \| \sqrt{I_{q_j}} - F\left[P_r \times O_{r+r_j} \right] \|^2, \quad \forall r_j \in S. \tag{8}$$

However, during the data acquisition process, the diffraction signals I_{q_j} are inevitably contaminated by the existing noise. The measured diffraction signals $I_{q_j}^{\mathrm{Meas}}$ can be obtained in practice as

$$I_{q_j}^{Meas} = \left| F\left[P_r \times O_{r+r_j} \right] \right|^2 + N_j(q), \quad \forall r_j \in S, \tag{9}$$

where, $N_j(q)$ are noise signals attached on the ideal diffraction signals I_{q_j}. Therefore, the problem of Eq. (8) is actually a complex non-convex optimization, and the minimum of the Euclidean norm has been transformed into the minimum of the density functional analysis $\varepsilon[N_j(q)]$

$$\min \varepsilon \left[N_j(q) \right] = \arg \min_{P_r, O_{r+r_j}} \sum_j \| \sqrt{I_{q_j}^{Meas}} - F\left[P_r \times O_{r+r_j} \right] \|^2, \quad \forall r_j \in S. \tag{10}$$

Usually, the noises in ptychography are mixed, not in a single form, mainly including the background noises (Direct-current distribution), the photon shot noises (Poisson distribution) and the reading noises (Gaussian distribution), etc., which are coupled with diffraction signals and seriously affect the convergence speed and reconstruction accuracy of iterative algorithms. Based on the ptychographic information multiplexing (PIM) algorithm [20] and the "Fractional" Fourier transform with Fresnel convolution integral [37], the proposed aNBS algorithm constructs the mixed noise density function by other virtual non-illumination wavelengths and synchronously updates the object function, the illumination probe and noise probes in the iteration loop, which adaptively blindly separates the coupled mixed noise into the virtual noise probes. The iteration steps of the algorithm are as follows:

1) Raw data acquisition. Raw measurement diffraction signals $I_{q_j}^{\mathrm{Meas}}$ are collected directly by CCD or CMOS cameras, and any pre-processing operations for raw signals need not to be done, where mixed noises are coupled in the raw data.
2) Initial guess of the object O_{r+r_j}, the illumination probe $P_r^{\mathrm{illu}}(\lambda_1)$ and the virtual noise probes $P_r^{\mathrm{nois}}(\lambda_n)$. Where, λ_1 is the illumination

wavelength and λ_n are other wavelengths. The matrix dimensions of the noise probes and the illumination probe are same, only the wavelengths are independent of each other.

3) Make the finite offsets S random. Cutting out the current area of the object O_{r+r_j}, which is identical in size to the probes, generates the exit-wave $\psi_r^{\mathrm{illu}}(\lambda_1)$ by interacting with the illumination probe $P_r^{illu}(\lambda_1)$. Noise probes $P_r^{\mathrm{nois}}(\lambda_n)$ do not interact with any objects, so exit-waves $\psi_r^{\mathrm{nois}}(\lambda_n)$ are themselves. Therefore, exit-waves with different wavelengths are expressed as

$$\begin{aligned} \psi_r^{\mathrm{illu}}(\lambda_1) &= P_r^{illu}(\lambda_1) \times O_{r+r_j}, \quad \forall r_j \in S, \\ \psi_r^{\mathrm{nois}}(\lambda_n) &= P_r^{nois}(\lambda_n), \quad n \geq 2. \end{aligned} \tag{11}$$

4) The exit-waves with different wavelengths are propagated by the "Fractional" Fresnel convolution integral, and the estimated diffraction distributions, including the illumination probe and noise probes, with different wavelengths can be expressed as

$$\Phi_q^{Est}(\lambda_n) = \mathfrak{F}[\psi_r(\lambda_n)], \quad n \geq 1, \tag{12}$$

where, $\mathfrak{F}$ is the "Fractional" Fourier transform with Fresnel convolution diffraction integral.

5) The modulus constraint at different wavelengths. Replace the estimated diffraction distribution with the measured raw data and keep the phases unchanged. The updated diffraction distributions $\Phi_q^{\mathrm{Est}'}(\lambda_n)$ can be obtained as

$$\Phi_q^{Est'}(\lambda_n) = \frac{\sqrt{I_{q_j}^{Meas}}}{\sqrt{\sum_n \left| \Phi_q^{Est}(\lambda_n) \right|^2}} \Phi_q^{Est}(\lambda_n), \quad n \geq 1 \tag{13}$$

6) The updated diffraction distributions are propagated by the inverse Fresnel convolution diffraction integral $\mathfrak{F}^{-1}$, the updated exit-waves $\psi_r'(\lambda_n)$ with different wavelengths are calculated as

$$\psi_r'(\lambda_n) = \mathfrak{F}^{-1}\left[\Phi_q^{Est'}(\lambda_n) \right], \quad n \geq 1, \tag{14}$$

and the object, the illumination probe and noise probes are also updated based on exit-waves before and after the update at the jth position in the set S

$$\begin{aligned} {}^{j+1}O_{r+r_j} &= {}^jO_{r+r_j} + \frac{{}^jP_r^{*illu}(\lambda_1)}{\alpha \left| {}^jP_r^{illu}(\lambda_1) \right|_{\max}^2 + (1-\alpha) \left| {}^jP_r^{illu}(\lambda_1) \right|^2} \left(\psi_r^{illu'}(\lambda_1) - \psi_r^{illu}(\lambda_1) \right), \quad \forall r_j \in S, \\ {}^{j+1}P_r^{illu}(\lambda_1) &= {}^jP_r^{illu}(\lambda_1) + \frac{{}^jO_{r+r_j}^{*}}{\beta \left| {}^jO_{r+r_j} \right|_{\max}^2 + (1-\beta) \left| {}^jO_{r+r_j} \right|^2} \left(\psi_r^{illu'}(\lambda_1) - \psi_r^{illu}(\lambda_1) \right), \quad \forall r_j \in S, \\ {}^{j+1}P_r^{nois}(\lambda_n) &= {}^jP_r^{nois}(\lambda_n) + \gamma \left(\psi_r^{nois'}(\lambda_n) - \psi_r^{nois}(\lambda_n) \right), \quad n \geq 2, \end{aligned} \tag{15}$$

where, α, β and γ are the step sizes between 0 and 1. In general, β and γ are larger than α [6] in the iteration process.

7) Take the updated object, illumination probe and noise probes as the initial guess of the j+1th position, and repeat steps 3)−6) until all positions in the set S have been traversed, in which case only one iteration is completed.
8) Repeat iterations N times until the algorithm converges.

Table 1
The aNBS ptychography algorithm for mixed noises.

Input:	Initial guess O_{r+r_j}, P_r^{illu} and P_r^{nois}, Shift set S and Raw data $I_{q_j}^{\text{Meas}}$
1	$\alpha,\ \beta,\ \gamma \in (0,1)\%$ Initial parameters
2	**for** $i = 1{:}N$
3	$K = \text{rand}(S)$ % Disorder randomly
4	**for** $j = 1{:}K$
5	$_i^j\psi_r^{\text{illu}} = {}_i^jP_r^{\text{illu}} \times {}_i^jO_{r+r_j},\ {}_i^j\psi_r^{\text{nois}} = {}_i^jP_r^{\text{nois}}$
6	$_i^j\Phi_q^{\text{illu}} = \mathfrak{F}({}_i^jP_r^{\text{illu}} \times {}_i^jO_{r+r_j}),\ {}_i^j\Phi_q^{\text{nois}} = \mathfrak{F}({}_i^jP_r^{\text{nois}})$
7	$_i^{j+1}\Phi_q^n = (\sqrt{I_{q_j}^{Meas}} / \sqrt{\sum_n |{}_i^j\Phi_q^n|^2})\,{}_i^j\Phi_q^n$
8	$_i^{j+1}\psi_r^{n'} = \mathfrak{F}^{-1}({}_i^{j+1}\Phi_q^n)$
9	$_i^{j+1}O_{r+r_j} = {}_i^jO_{r+r_j} + {}_i^jP_r^{*\text{illu}} /(\alpha|{}_i^jP_r^{\text{illu}}(\lambda_1)|_{\max}^2 + (1-\alpha)|{}_i^jP_r^{\text{illu}}(\lambda_1)|^2)(\psi_r^{\text{illu}'} - \psi_r^{\text{illu}})$
10	$_i^{j+1}P_r^{\text{illu}} = {}_i^jP_r^{\text{illu}} + {}_i^jO_{r+rj}^* /(\beta|{}_i^jO_{r+r_j}|_{\max}^2 + (1-\beta)|{}_i^jO_{r+r_j}|^2)(\psi_r^{\text{illu}'} - \psi_r^{\text{illu}})$
11	$_i^{j+1}P_r^{\text{nois}} = {}_i^jP_r^{\text{nois}} + \gamma(\psi_r^{\text{nois}'} - \psi_r^{\text{nois}})$
12	**End**
13	Auxiliary programs
14	**End**
Output:	Reconstruction object O_{r+r_j}, illumination probe P_r^{illu} and noise probes P_r^{nois}

The complete algorithm can be summarized as Table 1, and other details remain need to be considered to ensure the performance of the algorithm.

a) Compatibility with different ptychography algorithms. The aNBS algorithm for mixed noises is described in detail by an alternating projection based on the PIE kernel. In fact, the algorithm is also compatible with the reflection projection algorithms [7], proximal gradient algorithms [13], ADMM algorithms [16] and others [10].
b) Calibration of system parameters in ptychography. Calibration and compensation system parameters are the prerequisites for ensuring the convergence of ptychography. Therefore, the ptychography system parameters must be calibrated in advance by autofocusing strategy [21] for axial distance or by angle calibration method [22] for reflection ptychography in low-noise conditions.
c) Correction of translational position errors. To avoid the influence of translation position errors, or angle errors of the LED illumination in Fourier ptychography, on the convergence of the proposed algorithm, the cross-correlation method [23] is also applied in low-noise ptychography.

3. Numerical simulations

Numerical simulations were carried out to validate the performance of the proposed aNBS ptychography algorithm. A two-dimensional complex sample, referred to as the "object" in Fig. 1(a), was synthesized with the amplitude and phase derived from "Siemens" and "resChart", respectively. Similarly, the amplitude and phase of the "probe" were structured, where a parallel beam of 632.8 nm wavelength was propagated a finite distance in free space and then focused on the back focal plane by a 50 mm focal length lens. This complicated phase curvature requires increased robustness from the ptychography algorithm, bringing the numerical simulations closer to the physical reality. A 2048×2048 pixel camera collected 441 diffraction fields at a 50 mm position far from the object, and the object was driven in 21×21 grid sizes by the x-y translation stage with 20 pixels having 10% random offsets. Mixed noises with varying intensities were introduced into the diffraction fields to emulate coupled noises on ideal signals, taking into account the 16-bit dynamic range of the camera and 10^9 photon fluxes, where mixed noises intensities were quantified with the peak signal-to-noise ratio (PSNR).

In ptychographic imaging, noise rarely appears in a singular form. Instead, several types of mixed noise interact and interfere within ideal diffraction fields, and each ptychography algorithm has a different sensitivity to the different noise types and intensities [26,29,30]. Therefore, three mixed noises of 30 dB were added to raw signals, including the background noises coupled to Gaussian random noises (BG
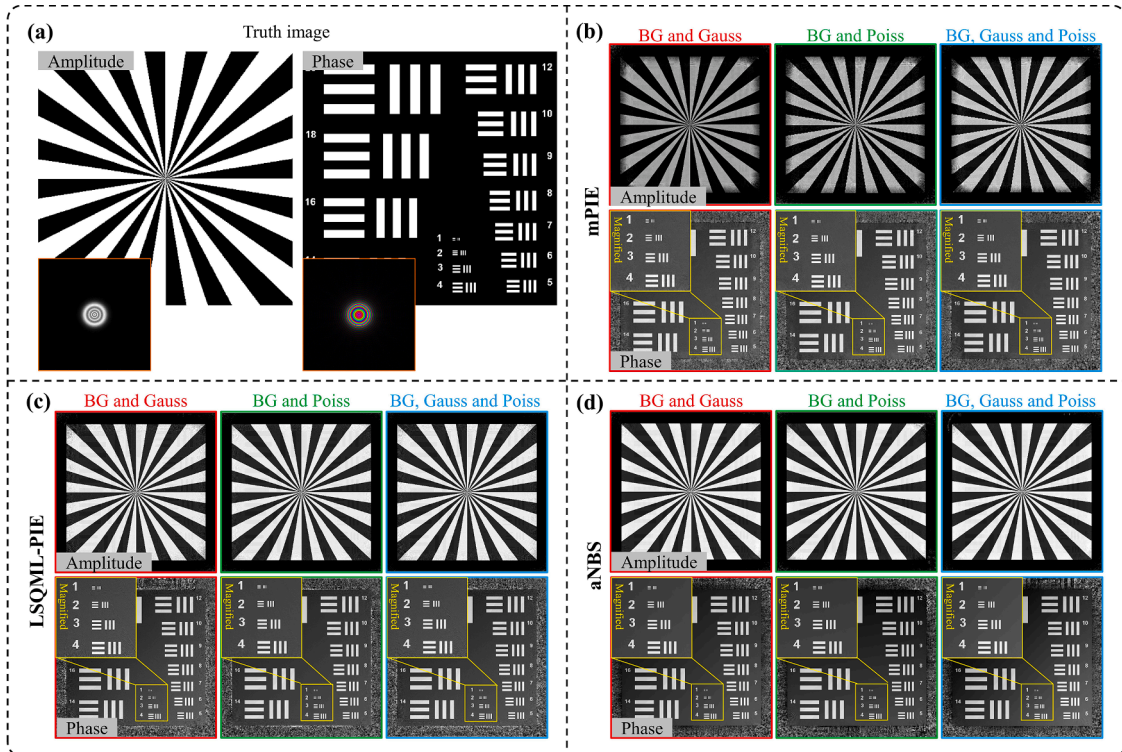
Fig. 1. Simulation results of different mixed noises with 30 dB noise intensity: (a) the amplitude and phase of the object and probe; (b) the mPIE algorithm; (c) the LSQML-PIE algorithm; (d) the aNBS ptychography algorithm.

and Gauss), the background noises coupled to Poisson random noises (BG and Poiss), and the background noises coupled to Gaussian-Poisson random noises (BG, Gauss and Poiss). After 500 iterations, the simulation results in Figs. 1(b)−1(d) show that the conventional mPIE algorithm exhibits perfect convergence performance in the three mixed noises scenarios. In particular, the line pair of Group 1 can be clearly distinguished in the results of each reconstruction phase image of the localized magnified views. In the case of the LSQML-PIE algorithm, the results also show remarkable reconstruction effects with clear amplitude and phase features identified. In addition, the image contrast is significantly better than that of the mPIE algorithm, which can be attributed to the noise optimization strategy provided by the mixed Poisson-Gaussian likelihood model in the LSQML-PIE algorithm. Finally, in the proposed aNBS ptychography algorithm, by establishing noise probes of the other wavelengths (594 nm and 543 nm) to blindly separate noise energies, the amplitude or phase images in Fig. 1(d) appear to the highest image contrast and sharpness than others. This is particularly evident in the minimally overlapping edge region, where no significant blurring is observed. Furthermore, for different mixed noise types, the proposed aNBS ptychography algorithm shows excellent feature uniformity, whereas the mPIE and LSQML-PIE algorithms exhibit minor sensitivity discrepancies.

When the signal-to-noise ratio of mixed noises intensities is reduced to 20 dB, the three ptychography algorithms undergo 500 iterations, and the results are shown in Fig. 2(a). Compared with the 30 dB low-intensity noises in Fig. 1(b), the mPIE algorithm appears pitch spots, especially at the edges, when background and Poisson random noises exist simultaneously, and the amplitude and phase patterns cross with each other. A similar phenomenon also occurs in the simulation results of the background, Gaussian and Poisson mixed noise. In contrast, the reconstruction results are more robust to background and Gaussian random noises in terms of convergence performance and image contrast, especially in the magnified views. In the reconstruction results of the LSQML-PIE algorithm, pitch spots are significantly reduced and cross-talk errors are slightly mitigated, especially in simulations involving mixed Gaussian-Poisson noise, but probe shape emerge that contaminate the amplitude and phase images at random locations. Similar to previous results, the LSQML-PIE algorithm does not assimilate Poisson random noise very well because it has the worst image contrast compared to other noise sources. However, owing to the superiority of the noise separation in the aNBS ptychography algorithm, the difference in feature uniformity and contrast of the images among the three mixed noises is negligible. The presence of both pitch spots and randomly positioned contaminating probes are effectively eliminated, causing reconstructed results that exhibit remarkable consistency and sharpness. Also, the proposed aNBS ptychography algorithm expresses more direct
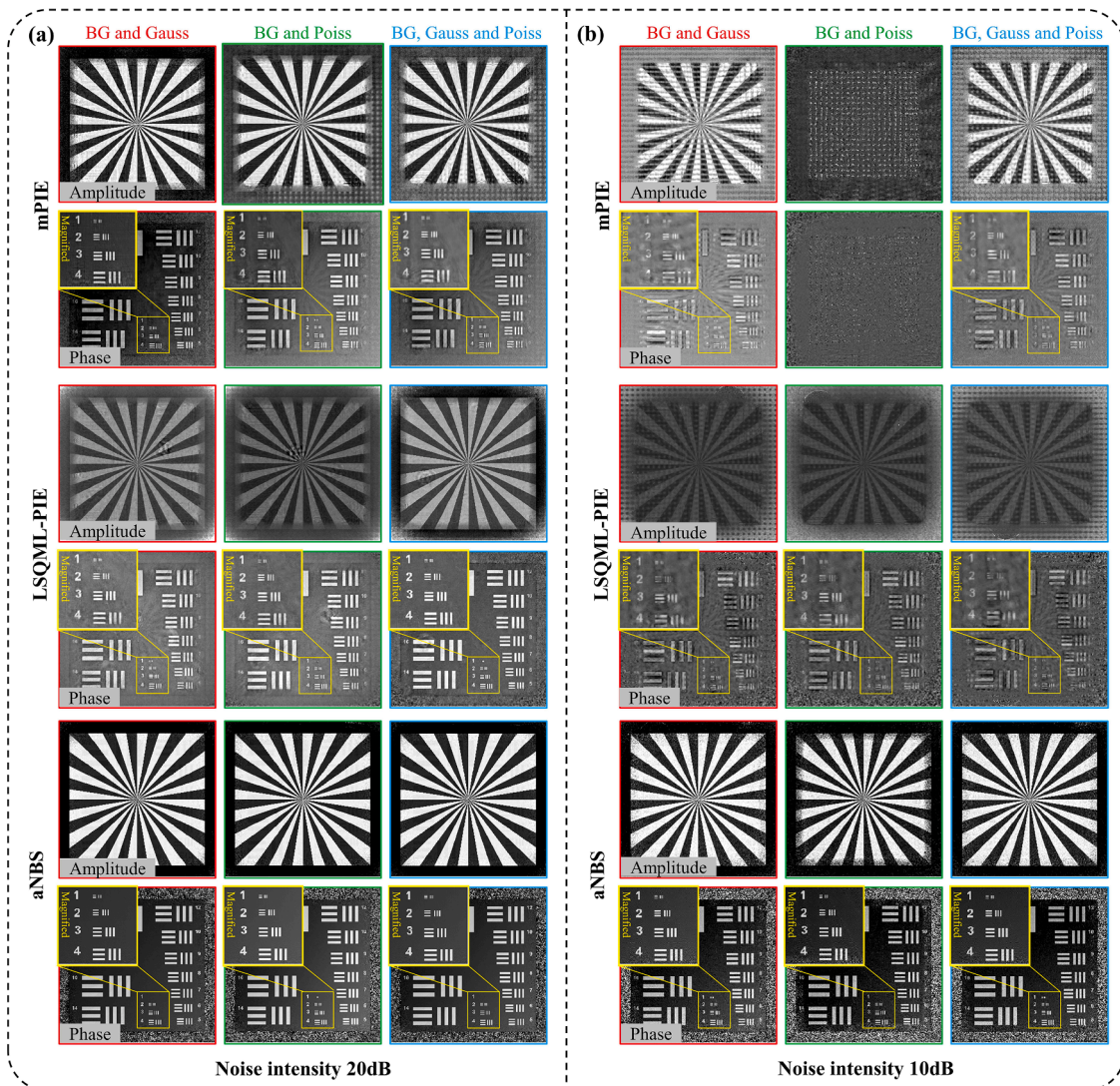

Fig. 2. Simulation experiments of different mixed noises: (a) the three algorithm reconstruction results with 20 dB noises intensity; (b) the three algorithm reconstruction results with 10 dB noises intensity.

response to sensitivity discrepancy to different mixed noise types.

When the mixed noise intensities are increased to 10 dB, the convergence performance of the three algorithms is presented in Fig. 2 (b). The proposed aNBS ptychography algorithm retains strong robustness despite the noise intensities increasing by two orders of magnitude, but the decrease in sharpness of the edges is apparent in all three different mixed noise scenarios. The results also observed when noise intensities were increased from 30 dB to 20 dB in mPIE and LSQML-PIE algorithms. This phenomenon can be attributed to the incomplete noise separation due to the limited number of noise probes in the aNBS algorithm. Also, regarding the iteration parameters, the updated step sizes (α, β, and γ) should be significantly smaller than low mixed noise intensities to avoid excessive oscillations. Finally, focusing on the performance of the mPIE and LSQML-PIE algorithms in high-intensity mixed noise environments, all reconstruction results are barely satisfactory or even extremely bad. In particular, the mPIE algorithm exhibits non-convergent iterative reconstruction results without any distinctive characteristics.

As the noise intensity increases, the reconstruction quality of images in mPIE algorithm gradually decreases until it fails, while the noise-optimization algorithm of LSQML-PIE shows a certain noise immunity but it shows selectivity for different mixed noise types. After noise intensity increases to a certain level, the LSQML-PIE algorithm also fails to converge. However, the proposed aNBS algorithm, due to its advantages of adaptive and blind noise separation based on the mixed state PIM algorithm [20], continues to converge robustly even when the noise intensity increases by two orders of magnitude. Furthermore, several image quality assessment techniques, including structural similarity (SSIM) and peak signal to noise ratio (PSNR) [44], were utilized to quantitatively assess the performance between the mPIE reference algorithm without any noises processing, the LSQML-PIE noise optimization algorithm and the proposed aNBS ptychographic algorithm. Figs. 3(a)−3(f) show the results of the "Siemens" amplitude image quality assessment, where the quantitative SSIM and PSNR metrics between the reconstruction images and the truth image confirm the qualitative observation results that the proposed aNBS ptychography algorithm provides superior reconstruction capabilities and exhibits negligible sensitivity discrepancy in the face of different mixed noise types. Furthermore, when the mixed noise intensities increase by two orders of magnitude in Table 2 (from 30 dB to 10 dB), the aNBS ptychography algorithm maintains its robust convergence and exhibits the same image convergence accuracy as the convention mPIE and the noise-optimization LSQML-PIE algorithm of 30 dB mixed noise. Identical results are observed in the phase reconstruction image of the "resChart" pattern, which will not be discussed in detail here.

In actually, both "Siemens" and "ResChart" are images of simple patterns with low information entropy. Assessing the reconstruction quality of an imaging algorithm is always inseparable from the complexity of the information entropy of the image itself. Therefore, whether the aNBS algorithm continues to maintain its highly robust convergence for specimens to be measured with complex information entropy is a question worth considering. Meanwhile, the introduction of image processing algorithms to improve the imaging resolution or noise immunity robustness of the aNBS algorithm is also not a bad choice either for future research.

4. Experiments

To verify the correctness of the simulation results, a general transmission geometry ptychography experimental setup was established as shown in Fig. 4(a), incorporating several additional optical elements such as optical filters, beam expanders, and irises, among others. The HeNe laser (Newport: N-STP-912) emitted a coherent beam with a wavelength of 632.8 nm with excellent energy and pointing fluctuations for the construction of the illumination probe. Photon flux and the radiation beam diameter ($1/e^2$) were modulated by optical filters, a beam expander (Thorlabs: GBE05-B), and a pinhole (Thorlabs: ID25Z) on the optical path in front of the focusing lens. Subsequently, a plano-convex lens (Newport: KPX049AR.14) with a focal length of 50 mm focused the modulated beam onto the back focal plane, where the illumination probe diameter was focused to approximately 150 μm. Simultaneously, a *x-y* translation stage (Physik Instrumente: Q-545.140) moved the
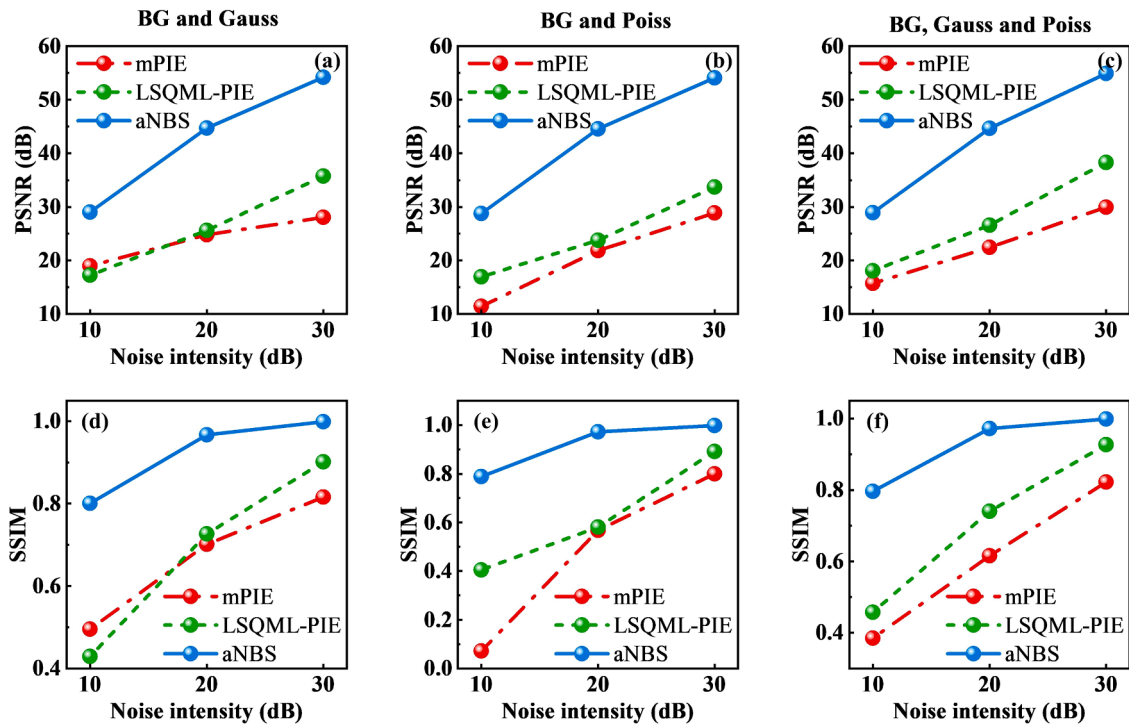

Fig. 3. The imaging quality assessment of three algorithms with different mixed noises (the amplitude image "Siemens"): (a)-(c) PSNR indicators; (d)-(f) SSIM indicators.

Table 2
The amplitude image quality assessment results for the "Siemens".

Algorithms	Mixed noises	30dB		20dB		10dB	
		PSNR	SSIM	PSNR	SSIM	PSNR	SSIM
mPIE	BG and Gauss	28.0216	0.8161	24.7574	0.7015	18.9523	0.4957
	BG and Poiss	28.8677	0.7992	21.8265	0.5677	11.4361	0.0719
	BG, Gauss and Poiss	29.9231	0.8221	22.4222	0.6155	15.6905	0.3849
LSQML-PIE	BG and Gauss	35.7380	0.9013	25.5863	0.7267	17.2410	0.4293
	BG and Poiss	33.6869	0.8917	23.7563	0.5807	16.9308	0.4044
	BG, Gauss and Poiss	38.2726	0.9271	26.5482	0.7406	18.0498	0.4572
aNBS	BG and Gauss	54.1673	0.9988	44.6886	0.9670	29.0063	0.8008
	BG and Poiss	54.0804	0.9985	44.5459	0.9720	28.7779	0.7888
	BG, Gauss and Poiss	54.9173	0.9988	44.6742	0.9724	28.9208	0.7959
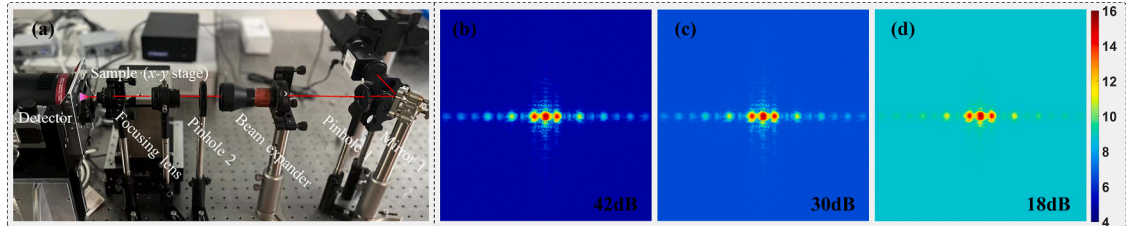
Fig. 4. The transmission geometry experimental setup and ptychographic raw data with different noise intensities: (a) general transmission geometry ptychography experimental setup; (b) 42 dB diffraction field; (c) 30 dB diffraction field. (d) 18 dB diffraction field.

USAF-1951 resolution target (Newport: RES-1) over 11×11 grids in the back focal plane. The grid interval was set to 20 μm with 10% random offsets to ensure more than 80% overlap. A 6280×4210 pixels astronomical CMOS camera (QHYCCD: QHY268M) with pixel size 3.76 μm and 16-bit dynamic range was positioned 13.9 mm away from the resolution target. The central photosensitive area of 4096×4096 pixels was cropped to collect 121 raw data points in the Extend Fullwell 2CMSIT mode. Meanwhile, 16×16 binning ($M \times N = 256 \times 256$ pixels image) was merged into the raw data to strike a balance between computational efficiency and the numerical aperture of the imaging system. Since the magnitude of mixed noises coupled in the diffraction signals could be dominated by the optical density of the optical filters and exposure times and offset factors of the CMOS detector, hence several optical experiments were set up with USAF-1951 as follows.

4.1. The amplitude specimen of resolution target USAF-1951

In order to obtain low mixed noises in the ptychographic raw data, an optical filter (Thorlabs: NE10A-A) with the optical density of 1.0 was chosen, and the camera was operated with an exposure time of 0.5 ms and an offset factor of 0. According to the general transmission geometry ptychography, the raw data with 42 dB mixed noises intensity were

collected in the CMOS camera shown in Fig. 4(b). Then in each experiment, the three algorithms were iterated 1000 times, keeping the algorithm parameters constant except for the number of noise probes in the aNBS algorithm. To solve more complex physical cases, an additional noise probe with a wavelength of 800 nm was added, and the experimental results are shown in Fig. 5. In agreement with the numerical simulation results, all algorithms demonstrate perfect convergence at a high signal-to-noise ratio, and the 2.2 μm line width features of Group 7/Element 6 is clearly observed in Fig. 5(a)–5(c). On closer inspection, the reconstruction results of the proposed aNBS ptychography algorithm in Fig. 5(c) exhibit the best sharpness and contrast for the line pair features and surrounding background region. The low overlap surrounding region of the images in Figs. 5(a) and 5(b) appear unclean for the mPIE and LSQML-PIE algorithms which use a single probe. Focusing on the line-pair features, the mPIE image has the worst feature uniformity and is more prominent random freckles than those in the LSQML-PIE image.

By reducing the signal-to-noise ratio of the raw data to a noise intensity of 30 dB, as shown in Fig. 4(c), using an optical filter (Thorlabs: NE20A-A) with optical density of 2.0, an exposure time of 2 ms, and an offset factor of 2 in the camera, the experimental results of the three ptychography algorithms are shown in Fig. 6. There is a negligible
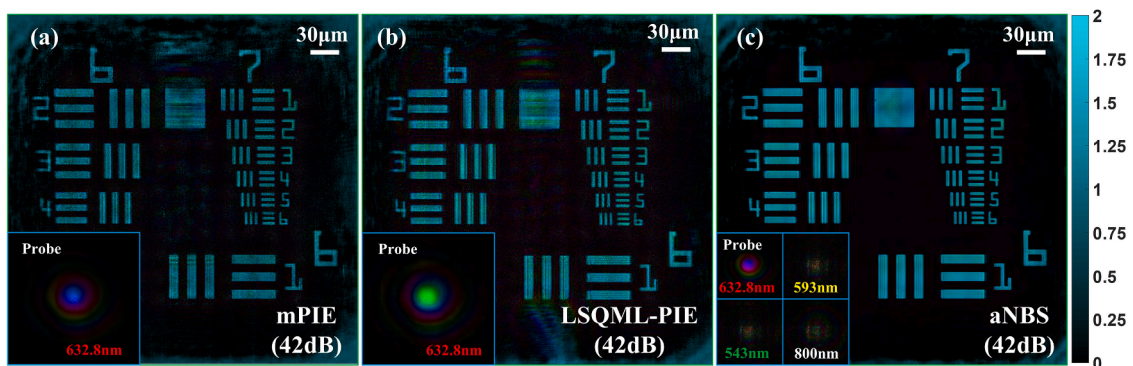
Fig. 5. Experiment results of resolution target USAF-1951 with 42 dB noise intensity: (a) the mPIE algorithm; (b) the LSQML-PIE algorithm; (c) the aNBS ptychography algorithm.
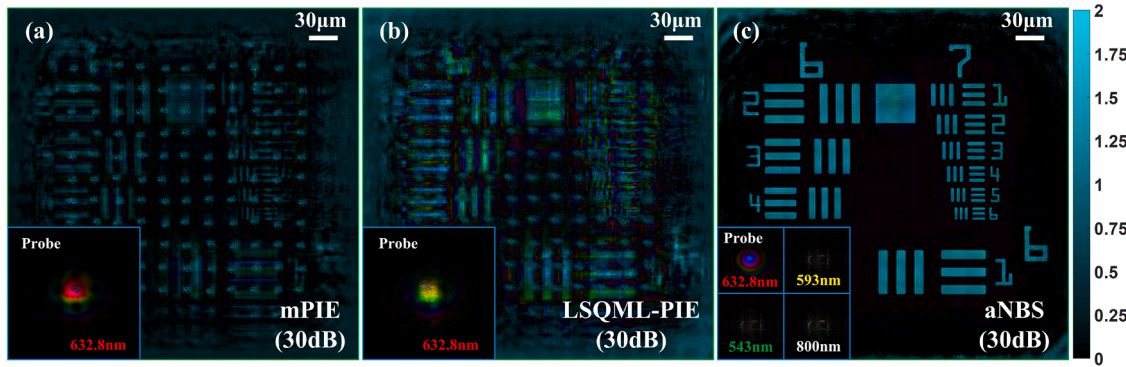
Fig. 6. Experiment results of resolution target USAF-1951 with 30 dB noise intensity: (a) the mPIE algorithm; (b) the LSQML-PIE algorithm; (c) the aNBS ptychography algorithm.
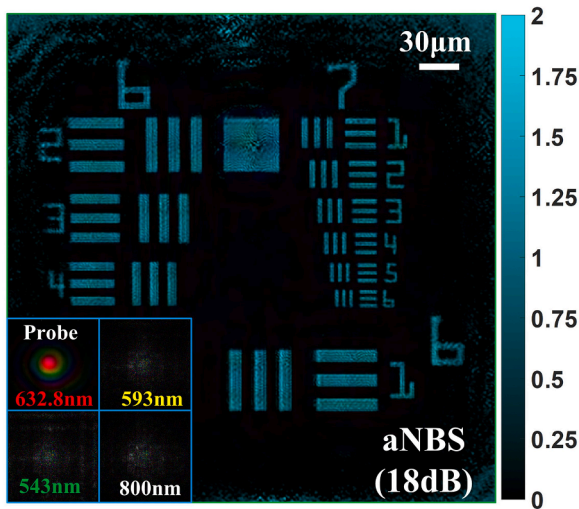
Fig. 7. Experimental results of the USAF-1951 resolution target with 18 dB noise intensity.

difference in the uniformity and contrast of the image features in Fig. 6 (c) compared with the image shown in Fig. 5(c). However, in Figs. 6(a) and 6(b), the quality of the reconstruction images deteriorates rapidly due to the presence of pitch-grid spots, resulting in the disappearance of the Group 7/Element 6 line pair from the image and the unusual shapes exhibited in the probe. A careful comparison with the mPIE algorithm shows that larger line pair features are easier to identify in the LSQML-PIE image, such as Group 6/Element 3 or larger others.

By further using an exposure time of 10 ms, an offset factor of 50, and an optical density filter of 3.0 (Thorlabs: NE30A-A) in the experiment to increase the magnitude of mixed noises to 18 dB as shown in Fig. 4(d), the mPIE and LSQML-PIE algorithms fail to converge and the results are not shown in detail here. The proposed aNBS ptychography algorithm maintains robust convergence for mixed noises, where the abundant random freckles appear on line pair features and surrounding region in Fig. 7 relative to Figs. 5(c) and 6(c) despite four noise probes are setup in the iteration process. Without considering computational efficiency, it may be a valuable move to continuously increase the number of noise probes to address the random freckle contamination in the images.

In comparison with the mPIE and LSQMI-PIE algorithms, both numerical simulations and experimental results demonstrate that the proposed mixed noises aNBS ptychography algorithm effectively eliminates random pixel freckles and pitch spots in features and surrounding regions, while the reconstructed images show the best sharpness and contrast at low and moderate mixed noise intensities. Meantime, the reconstruction results of the aNBS ptychography algorithm show no

image blurring at different mixed noise levels. Especially in real physical experiments, it is often difficult to determine whether multiple noises are coupled with each other or which type of noise mainly affects the results. The proposed aNBS ptychography algorithm still has excellent convergence robustness and negligible sensitivity difference for different mixed noise types.

All the superior results in the simulations and experiments can be attributed to the fact that the aNBS algorithm constructs additional virtual probes to load the noise energies, which can adaptively blind separate coupling mixed noises into the virtual noise probes in ptychography based on the mixed state PIM algorithm [20]. Further focusing on the case of low signal-to-noise ratio, the proposed aNBS ptychography algorithm exhibits more than two orders of magnitude improvement in noise intensity immunity compared with other non-separated noise ptychography algorithms without requiring additional regularization constraints or noise prior assumptions. An important aspect to consider in the aNBS algorithm is that the iteration parameters should be smaller for medium and high signal-to-noise data, as smaller step sizes can help avoid iterative oscillations and facilitate easier convergence orientation [31].

4.2. The biological specimen of human hematocyte smear

The USAF-1951 resolution target, being a familiar amplitude specimen only, does not fully reflect the superiority of the ptychography algorithm. To validate the proposed aNBS ptychography algorithm in addressing mixed noises, complex human hematocyte smear with more information entropy was used in a ptychography experiment. The experiment setup of the transmission geometry was similar to that of the USAF-1951 ptychography device with a noise intensity of 32 dB, except that the distance (14.4 mm) between the detector and the biological specimen was varied due to self-thickness of the specimen. The reconstructed amplitude and phase images of the object and the probes are shown in Figs. 8(a) and 8(b). In reconstruction results of the regions (a_1)-(b_1) and (a_2)-(b_2), structural features are clearly distinguishable in the phase image, whereas they appear blurred in the amplitude image of the
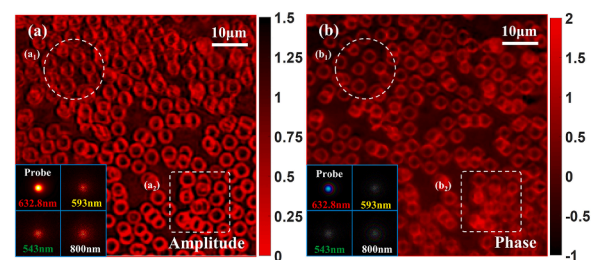
Fig. 8. Experimental results of the aNBS ptychography algorithm on a biological sample with 32 dB noise intensity: (a) amplitude; (b) phase.

corresponding area, and vice versa. The complementary imaging helps to eliminate the influence of different factors on the ptychography results.

Compared with the amplitude specimen USAF-1951 experiments, the reconstruction experiment of the biological specimen demonstrates that the proposed mixed-noise aNBS ptychography algorithm has good robustness for complicated phase specimens. The imaging results between amplitude and phase reconstructions complement each other well, especially in providing detailed information about the specimen, such as in the case of non-uniform staining in cells or multiple cells stacked together, which can obscure the amplitude or phase imaging results. The aNBS ptychography method, with its noise blind separation and system error calibration capabilities, provides the most intuitive representation of the physical reality of the specimen, ensuring that any image quality issues can be attributed to the specimen itself rather than external factors. This highlights the advantage of ptychography imaging in complex biological specimens.

5. Conclusion

In summary, a novel aNBS ptychography algorithm is proposed to address mixed noises of different types without sensitivity discrepancy. Firstly, a variable scale Fresnel convolution integral based on the "Fractional" Fourier transform was introduced to gracefully resolve scale constraints between the sampling interval and optical field size over different wavelengths in optical propagation. Then, virtual probes different from the illumination probe were also innovatively constructed to capture the noise energies, enabling the adaptive blind separation of mixed noises from coupled raw ptychographic signals. Finally, through simulations and experiments, the effectiveness and correctness of the aNBS-based ptychography method had quantitatively and qualitatively been validated. Results indicate that the proposed algorithm maintains robust convergence even as the noise intensity increases by over two orders of magnitude compared with existing approaches. More importantly, the algorithm does not depend on noise prior assumptions, regularization constraints, and dynamic iteration parameters during the iterative process, which make it more robust and general than state-of-the-art ptychographic noise-suppression algorithms.

There is also a critical issue that needs to be concerned in the future, that is, how to further improve the robustness at higher noise levels without sacrificing the computational efficiency in phase retrieval. These potential strategies should be considered, including increasing the number of additional noise probes, designing special virtual samples, incorporating proper regularization [6,17], or implementing other approaches [10,32,45] in the aNBS algorithm.

CRediT authorship contribution statement

Li Liu: Conceptualization, Methodology, Validation, Software, Investigation, Writing – original draft, Writing – review & editing, Resources, Formal analysis, Data curation. **Wenjie Li:** Software, Investigation, Writing – original draft, Writing – review & editing. **Lei Zhong:** Resources, Formal analysis, Data curation. **Honggang Gu:** Conceptualization, Methodology, Validation, Writing – review & editing, Supervision, Project administration, Funding acquisition. **Shiyuan Liu:** Writing – review & editing, Supervision, Project administration, Funding acquisition.

Declaration of Competing Interest

The authors declare that they have no known competing financial interests or personal relationships that could have appeared to influence the work reported in this paper.

Data availability

Data will be made available on request.

References

[1] Gao S, Wang P, Zhang F, Martinez GT, Nellist PD, Pan X, et al. Electron ptychographic microscopy for three-dimensional imaging. Nat Commun 2017;8(1): 1–8.

[2] Donnelly C, Guizar-Sicairos M, Scagnoli V, Holler M, Huthwelker T, Menzel A, et al. Element-specific X-ray phase tomography of 3D structures at the nanoscale. Phys Rev Lett 2015;114:.11:115501.

[3] Tanksalvala M, Porter CL, Esashi Y, Wang B, Jenkins NW, Zhang Z, et al. Nondestructive, high-resolution, chemically specific 3D nanostructure characterization using phase-sensitive EUV imaging reflectometry. Sci Adv 2021;7 (5):eabd9667.

[4] Rodenburg JM, Faulkner HML. A phase retrieval algorithm for shifting illumination. Appl Phys Lett 2004;85(20):4795–7.

[5] Maiden AM, Rodenburg JM. An improved ptychographical phase retrieval algorithm for diffractive imaging. Ultramicroscopy 2009;109(10):1256–62.

[6] Maiden A, Johnson D, Li P. Further improvements to the ptychographical iterative engine. Optica 2017;4(7):736–45.

[7] Thibault P, Dierolf M, Bunk O, Menzel A, Pfeiffer F. Probe retrieval in ptychographic coherent diffractive imaging. Ultramicroscopy 2009;109(4):338–43.

[8] Luke DR. Relaxed averaged alternating reflections for diffraction imaging. Inverse Probl 2004;21(1):37–50.

[9] Fannjiang A, Zhang Z. Fixed Point Analysis of Douglas–Rachford Splitting for Ptychography and Phase Retrieval. SIAM J Imaging Sci 2020;13(2):609–50.

[10] Pham M, Rana A, Miao J, Osher S. Semi-implicit relaxed Douglas-Rachford algorithm (sDR) for ptychography. Opt Express 2019;27(22):31246–60.

[11] Marchesini S. Invited article: A unified evaluation of iterative projection algorithms for phase retrieval. Rev Sci Instrum 2007;78(1):011301.

[12] Yan H. Ptychographic phase retrieval by proximal algorithms. New J Phys 2020;22 (2):023035.

[13] Huang Y, Jiang S, Wang R, Song P, Zhang J, Zheng G, et al. Ptychography-based high-throughput lensless on-chip microscopy via incremental proximal algorithms. Opt Express 2021;29(23):37892–906.

[14] Hesse R, Luke DR, Sabach S, Tam MK. Proximal heterogeneous block implicit-explicit method and application to blind ptychographic diffraction imaging. SIAM J Imaging Sci 2015;8(1):426–57.

[15] Wang A, Zhang Z, Wang S, Pan A, Ma C, Yao B. Fourier Ptychographic Microscopy via Alternating Direction Method of Multipliers. Cells 2022;11(9):1512.

[16] Chang H, Enfedaque P, Marchesini S. Blind ptychographic phase retrieval via convergent alternating direction method of multipliers. SIAM J Imaging Sci 2019; 12(1):153–85.

[17] Wu J, Yang F, Cao L. Resolution enhancement of long-range imaging with sparse apertures. Opt Lasers Eng 2022;155:107068.

[18] Rodenburg J, Maiden A. Ptychography springer handbook of microscopy, hawkes pw and spence JCH,. Switzerland: Springer Nature; 2019. p. 819–904.

[19] Thibault P, Menzel A. Reconstructing state mixtures from diffraction measurements. Nature 2013;494(7435):68–71.

[20] Batey DJ, Claus D, Rodenburg JM. Information multiplexing in ptychography. Ultramicroscopy 2014;138:13–21.

[21] Loetgering L, Du M, Eikema KSE, Witte S. zPIE: an autofocusing algorithm for ptychography. Opt Lett 2020;45(7):2030–3.

[22] Beurs A, Loetgering L, Herczog M, Du M, Eikema KSE, Witte S. aPIE: an angle calibration algorithm for reflection ptychography. Opt Lett 2022;47(8):1949–52.

[23] Zhang F, Peterson I, Vila-Comamala J, Diaz A, Berenguer F, Bean R, et al. Translation position determination in ptychographic coherent diffraction imaging. Opt Express 2013;21(11):13592–606.

[24] Maiden AM, Humphry MJ, Rodenburg JM. Ptychographic transmission microscopy in three dimensions using a multi-slice approach. J Opt Soc Am A 2012;29(8): 1606–14.

[25] Thibault P. Guizar-Sicairos M. Maximum-likelihood refinement for coherent diffractive imaging. New J Phys 2012;14(6):063004.

[26] Odstrčil M, Menzel A. Guizar-Sicairos M. Iterative least-squares solver for generalized maximum-likelihood ptychography. Opt Express 2018;26(3):3108–23.

[27] Yeh LH, Dong J, Zhong J, Tian L, Chen M, Tang G, et al. Experimental robustness of Fourier ptychography phase retrieval algorithms. Opt Express 2015;23(26): 33214–40.

[28] Bian L, Suo J, Chung J, Ou X, Yang C, Chen F, et al. Fourier ptychographic reconstruction using Poisson maximum likelihood and truncated Wirtinger gradient. Sci Rep 2016;6(1):1–10.

[29] Chang H, Lou Y, Duan Y, Marchesini S. Total variation based phase retrieval for Poisson noise removal. SIAM J Imaging Sci 2018;11(1):24–55.

[30] Zhang Y, Song P, Dai Q. Fourier ptychographic microscopy using a generalized Anscombe transform approximation of the mixed Poisson-Gaussian likelihood. Opt Express 2017;25(1):168–79.

[31] Konijnenberg AP, Coene WMJ, Urbach HP. Model-independent noise-robust extension of ptychography. Opt Express 2018;26(5):5857–74.

[32] Zuo C, Sun J, Chen Q. Adaptive step-size strategy for noise-robust Fourier ptychographic microscopy. Opt Express 2016;24(18):20724–44.

[33] Wu X, Zhao J, Cui G, Mao H. A lensless LED matrix-based ptychographic microscopy imaging method using loss correction and adaptive step size. Opt Lasers Eng 2022;152:106980.

[34] Wang C, Xu Z, Liu H, Wang Y, Wang J, Tai R. Background noise removal in x-ray ptychography. Appl Optics 2017;56(8):2099–111.

[35] Qiao Z, Wen X, Zhou X, Qin F, Liu S, Gao B, et al. Adaptive iterative guided filtering for suppressing background noise in ptychographical imaging. Opt Lasers Eng 2023;160:107233.

[36] Chang H, Enfedaque P, Zhang J, Reinhardt J, Enders B, Yu YS, et al. Advanced denoising for X-ray ptychography. Opt Express 2019;27(8):10395–418.

[37] Muffoletto RP, Tyler JM, Tohline JE. Shifted Fresnel diffraction for computational holography. Opt Express 2007;15(9):5631–40.

[38] Wittwer F, Hagemann J, Brückner D, Flenner S, Schroer CG. Phase retrieval framework for direct reconstruction of the projected refractive index applied to ptychography and holography. Optica 2022;9(3):295–302.

[39] Zheng G. Fourier ptychographic imaging: a MATLAB® tutorial. San Rafael: Morgan & Claypool Publishers; 2016.

[40] Zürch MW. High-Resolution extreme ultraviolet microscopy: imaging of artificial and biological specimens with laser-driven ultrafast xuv sources. Switzerland: Springer International Publishing; 2015.

[41] Raines KS, Salha S, Sandberg RL, Jiang H, Rodríguez JA, Fahimian BP, et al. Three-dimensional structure determination from a single view. Nature 2010;463(7278): 214–7.

[42] Mutzafi M, Shechtman Y, Eldar YC, Cohen O, Segev M. Sparsity-based Ankylography for Recovering 3D molecular structures from single-shot 2D scattered light intensity. Nat Commun 2015;6(1):1–8.

[43] Voelz DG. Computational fourier optics: a MATLAB® tutorial. Bellingham: Society of Photo-Optical Instrumentation Engineers (SPIE); 2011.

[44] Chang X, Jiang S, Hu Y, Zheng G, Bian L. Pixel super-resolved lensless on-chip sensor with scattering multiplexing. ACS Photonics 2023;10(7):2323–31.

[45] Ivanović VN, Brnović NR. Superior Execution Time Design of a Space/Spatial-Frequency Optimal Filter for Highly Nonstationary 2D FM Signal Estimation. IEEE Trans Circuit Syst I-Regul Pap 2018;65(10):3376–89.